Tracing life through light: towards detecting life on exoplanets with spectroscopy and spectropolarimetry

Mulder, W.

Part I

Characterising atmospheres through spectroscopy

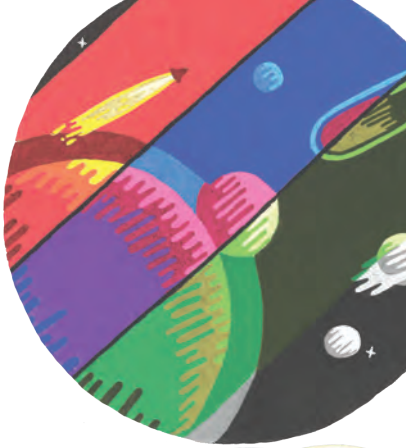

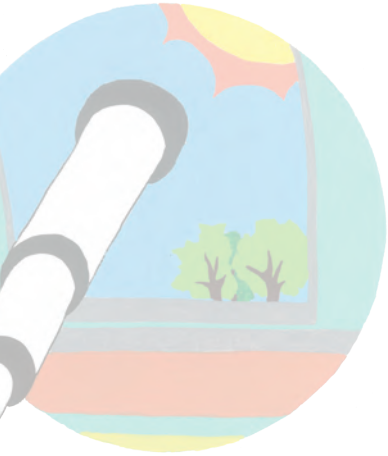

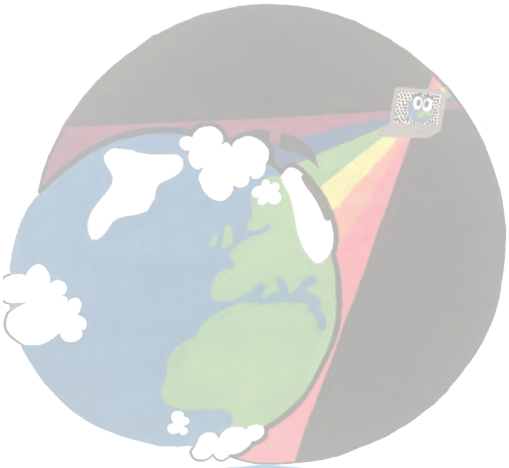

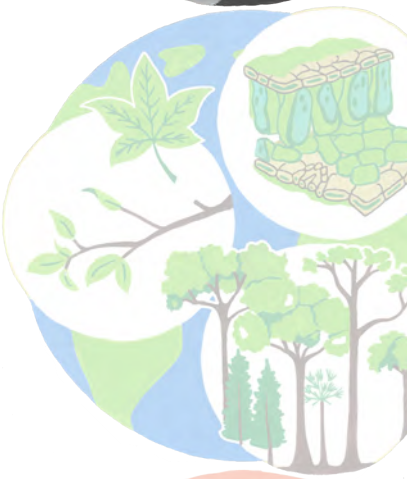


ANGRY
PHOTONS


THE
BEETLES

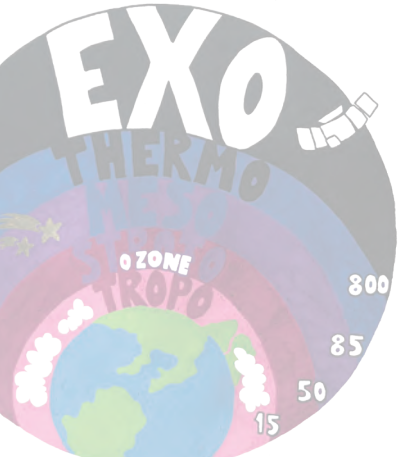
EXO
THERMO
OZONE
800
85
50
15

2 | Atmospheric characterisation of brown dwarf atmospheres

Published as

The ESO SupJup Survey VI:
$^{12}C/^{13}C$ isotope ratio comparison of three L-type brown dwarfs

W. Mulder, S. de Regt, R. Landman, D. González Picos, I. A. G. Snellen, Y. Zhang, S. Gandhi, C. Ginski, A. Y. Kesseli, P. Mollière, E. Nasedkin, and T. Stolker

Astronomy & Astrophysics, 694, A164 (2025)

Recent research suggests that the distinct formation processes of exoplanets and brown dwarfs may have an influence on the chemical and isotopic composition of their atmospheres. Variations in the carbon $^{12}C/^{13}C$ isotope ratio have been observed and tentatively linked to the top-down formation of brown dwarfs and the core accretion pathway of super-Jupiters. The European Southern Observatory SupJup Survey, conducted with CRIRES+ on the Very Large Telescope, aims to characterise the atmospheres of young brown dwarfs and super-Jupiters, specifically by investigating the $^{12}C/^{13}C$ ratio as a tracer of their formation pathways. We present the atmospheric characterisation of three isolated L-type brown dwarfs (2MASS J08354256-0819237, 2MASS J05012406-0010452, and 2MASS J05002100+0330501) included in the ESO SupJup Survey. We aim to constrain the C/O and $^{12}C/^{13}C$ ratios, and investigate whether the oxygen $^{16}O/^{18}O$ isotope ratio can be probed. We analysed the CRIRES+ K-band spectra of the three targets using our atmospheric retrieval framework. This framework couples the radiative transfer code `petitRADTRANS` with the sampling algorithm `MultiNest`. We report $^{12}C/^{13}C$ ratios of 89^{+11}_{-11} and 117^{+20}_{-17} for J0835 and J0500 with strong ^{13}CO significance ($> 6.8\sigma$) and a tentative (3σ) detection of ^{13}CO for J0501, resulting in a carbon isotope ratio of 155^{+56}_{-53}. Only a weak detection of the $H_2^{18}O$ isotope was found in J0835. The C/O ratios are found to be in the range 0.65 to 0.71 for the three targets, and all exhibit strong detections of hydrogen fluoride. The $^{12}C/^{13}C$ ratios appear to be higher than that of the interstellar medium.

2.1 Introduction

Spectroscopic observations of exoplanetary atmospheres allow us to trace their chemical compositions and determine their thermal structure and possible cloud properties (Janson et al., 2010; Barman et al., 2011; Currie et al., 2011; Skemer et al., 2012; Oppenheimer et al., 2013). In addition to providing information about their atmospheric conditions, such a characterisation may help in constraining exoplanet formation and evolutionary processes. High-resolution spectroscopy plays an important role in unveiling the intricacies of exoplanet atmospheres, as it unequivocally determines the presence (Brogi et al., 2012; Hoeijmakers et al., 2020) and abundances (Brogi & Line, 2019; Line et al., 2021) of molecular and atomic species, as well as atmospheric dynamics (Brogi et al., 2016; Snellen et al., 2014; Schwarz et al., 2016).

The chemical composition of planetary atmospheres is believed to be linked to local formation conditions (Mollière et al., 2022). The chemical abundance ratios may deviate from that of the interstellar medium (ISM) and are governed by the material (gas or ice) they accrete from their environment during formation. As a result, various chemical abundance ratios have been suggested as tracers of planet formation. One planet formation tracer that is commonly studied is the carbon-to-oxygen (C/O) ratio (Öberg et al., 2011; Madhusudhan et al., 2010; Madhusudhan, 2012). The local C/O ratio in a protoplanetary disk is likely affected by various snow lines (Piso et al., 2015), namely of H_2O, CO, and CO_2, which determine whether these molecular species are generally present as ices or in the gas phase. This will subsequently influence the chemical buildup of the planets that form. Other chemical abundance ratios that have been suggested as formation and evolution tracers are, for example, the nitrogen-to-oxygen (N/O) or nitrogen-to-carbon ratio (N/C) for hot Jupiters (Cridland et al., 2016) and gas giants (Turrini et al., 2021), as well as the refractory-to-volatile ratio for ultra-hot Jupiters (Lothringer et al., 2021).

Isotope ratios have also been proposed as potential tracers of planetary formation history and evolution (Clayton & Nittler, 2004; Mollière et al., 2019; Zhang et al., 2021). The deuterium-to-hydrogen (D/H) ratio in our Solar System is of importance for our understanding of the origin and evolution of water within our celestial neighbourhood. In contrast to D/H ratios, the carbon isotope ratio is roughly constant (~89) in the Solar System (Woods & Willacy, 2009); however, it varies on galactic scales as ^{13}C is produced within stars that enrich the ISM over time. The current local ISM has an average isotopologue ratio of 68 ± 15 (Langer & Penzias, 1993; Milam et al., 2005), significantly lower than that of the Solar System. Interestingly, isotope fractionation processes create variations on protoplanetary disk scales (Woods & Willacy, 2009), which could be passed on to exoplanet atmospheres. (Zhang et al., 2021; Mollière et al., 2019; Line et al., 2021; Bergin et al., 2024).

Young brown dwarfs (BDs) closely resemble super-Jupiters (SJs) in terms of atmospheric characteristics, but are significantly more observationally accessible. This makes them highly valuable for spectroscopic studies. Formed with high temperatures and inflated radii, these self-luminous objects subsequently cool and undergo gravitational contraction, meaning that they are particularly amenable to detailed spectroscopic observations at a young age. Recent advancements in atmospheric retrieval techniques enable the quantitative characterisation of both young BDs and SJs, taking advantage of instruments such as the upgraded Cross-

dispersed hIgh-Resolution Infrared Spectrograph (CRIRES+; Dorn et al., 2023) and the Keck Planet Imager and Characterizer (KPIC; Delorme et al., 2021; Wang et al., 2021; Xuan et al., 2022), along with space-based facilities such as the James Webb Space Telescope (JWST; Gandhi et al., 2023).

(Isolated) BDs are believed to form similarly to stars, through the collapse of molecular clouds (Bate et al., 2002; Whitworth et al., 2007), while giant planets such as SJs can follow distinct formation pathways that involve solid and gas accretion (Pollack et al., 1996; Helled et al., 2014). Reliable measurements of chemical abundance (C/O) and isotopic ($^{12}C/^{13}C$) ratios in representative samples of BDs and SJs could provide crucial insights into these formation processes.

This chapter is organised as follows. In section 2.2 we summarise the main characteristics of our sample of BDs taken from literature. Section 2.3 addresses the CRIRES+ observations of the BD sample and the corresponding data reduction. Section 2.4 discusses our forward modelling and the atmospheric retrieval framework. In section 2.5 the main results of the retrievals are reported, and we discuss the implications of our findings in the context of young BDs and recent literature on C/O and isotope ratios. Finally, section 5.6 summarises our conclusions.

2.2 Sample selection

In this chapter we present high-resolution spectra of three isolated L-type BDs: 2MASS J08354256-0819237, 2MASS J05012406-0010452, and 2MASS J05002100+0330501. These objects were selected from the European Southern Observatory SupJup Survey (programme ID 1110.C-4264, PI: Snellen), which aims to compare the atmospheres of sub-stellar companions and isolated BDs (de Regt et al., 2024; González Picos et al., 2024). The complete sample consists of 49 targets, ranging from early M-type stars to cool T-dwarfs (see Fig. 2.1). Ultimately, we aim to run retrievals for all objects in the sample.

The three BDs selected for this study have similar spectral types (L4.0-5.0) and effective temperatures ($T_{\rm eff}$ =1700 − 1800K), which allows a comparison between atmospheres at comparable conditions. As a result, differences in the atmospheric chemistry between the BDs could possibly inform us of distinct formation scenarios. In addition, the presented constraints for these isolated BDs can serve for comparison with planetary-mass companions in a similar temperature regime (Zhang et al., 2021; Zhang et al., 2021). The probed effective temperatures are typical for sub-stellar L-type objects ($T_{\rm eff}$ = 1300 – 2200K, Filippazzo et al. 2015) and allow the formation of mineral and metal condensate clouds in their atmospheres (Tsuji et al., 1996; Visscher et al., 2010). We refer to Table 2.1 for more detailed properties of the studied BDs.

2.2.1 J0835

2MASS J08354256-0819237 (J0835 hereafter) is an isolated L-type BD. Its spectral type, based on photometry, is L5.0 Cruz et al. (2003); Burgasser et al. (2010); Andrei et al. (2011). Previous work used various methods to estimate the effective temperature of J0835, reporting 2200 K (Blake et al., 2010), 1800 ± 100 K (Gagné et al., 2015), 1754 ± 112 K (Filippazzo

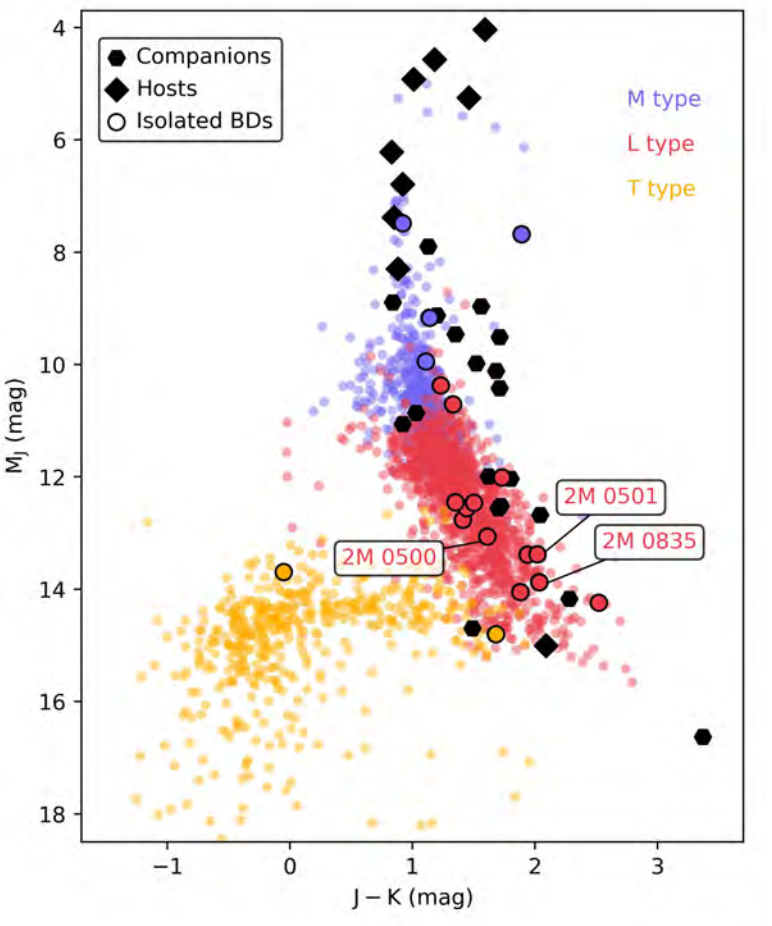

Figure 2.1: Colour-magnitude diagram of M_J vs $J - K$ showing the observed low- and planetary-mass objects of the ESO SupJup Survey. The companions and their hosts are pictured as black hexagons and diamonds, respectively. All 19 observed isolated BDs are marked as black-outlined circles, and the colour denotes their spectral type. The same colour coding is used for the population of isolated cool dwarfs indicated in the background. These objects, originating from the `UltracoolSheet` (Best et al., 2024), are shown as a reference.

System name	Distance (pc)	Spectral type	T_{eff} (K)	Mass (M_{Jup})	Radius (R_{Jup})	$v \sin i$ (km s^{-1})	i (°)
J0835	$7.23 \pm 0.01^{(1)}$	L5.0$^{(2)}$	$1754 \pm 112^{(4)}$	$62.47 \pm 15.86^{(6)}$	$1.00 \pm 0.08^{(6)}$	$9.65 \pm 0.36^{(7)}$	$21^{(4)}$
J0501	$20.9 \pm 0.3^{(1)}$	L4.0$\gamma^{(5)}$	$1720 \pm 55^{(5)}$	$21.45 \pm 13.71^{(6)}$	$1.38 \pm 0.18^{(6)}$	$9.57^{+0.67\,(7)}_{-0.58}$	$60^{+20(4)}_{-9}$
J0500	$13.23 \pm 0.05^{(1)}$	L4.0 pec C$^{(3)}$	$1793 \pm 72^{(6)}$	$63.68 \pm 14.44^{(6)}$	$1.00 \pm 0.08^{(6)}$	$9.57^{+0.67\,(8)}_{-0.58}$	—

Table 2.1: Properties of our L-type BD sample: (1) Gaia Collaboration (2020), (2) Cruz et al. (2003), (3) Gagné et al. (2015), (4) Schlawin et al. (2017), (5) Zapatero Osorio et al. (2014), (6) Filippazzo et al. (2015), (7) Vos et al. (2020), (8) Blake et al. (2010).

System name	RA	Dec.	Obs. date (UT)	K (mag)	iTime (s)	S/N	Seeing(")	Std star
J0835	08 35 42.53	-08 19 15.85	2023-01-02	$11.14 \pm 0.02^{(5)}$	1200	70	~0.7	pi.05 Ori
J0501	05 01 24.09	-00 10 49.19	2023-02-02	$12.96 \pm 0.04^{(5)}$	3600	20	~0.8	HD 31331
J0500	05 00 21.01	03 30 45.40	2023-02-28	$12.06 \pm 0.02^{(5)}$	5400	40	~0.7	3 Hya

Table 2.2: Observational parameters for the three L-type BDs: The parameters include observation date, apparent K-band magnitudes from the 2MASS catalogue (Cutri et al., 2003), total integration time, S/N at 2166nm, and standard star used for telluric corrections.

et al., 2015; Schlawin et al., 2017) and 1374 ± 52 K (Sanghi et al., 2023). Blake et al. (2010) based their $T_{\rm eff}$ on a best-fit synthetic template with $\log g = 5.0$, Gagné et al. (2015) fitted a model using WISE W1 and W2 photometry as well as near-infrared (NIR) spectra in the J-, H-, and K-bands, Filippazzo et al. (2015) used the bolometric luminosity, and Sanghi et al. (2023) combined their own observations and evolutionary model-derived radii to determine semi-empirical effective temperatures.

Gagné et al. (2015) reported no clear signatures of low surface gravity. They determined a surface gravity of $\log g = 5.0 \pm 0.5$ using optically anchored NIR spectral average templates. Subsequently, Filippazzo et al. (2015) noted a similar surface gravity of $\log g_{\rm J0835} = 5.19 \pm 0.21$. In general, low surface gravity BDs are thought to be younger objects with inflated radii, which has been confirmed in previous work (e.g. Kirkpatrick et al., 2008; Liu et al., 2016; Schlawin et al., 2017). Young BDs stand out because of their redder NIR and mid-infrared (MIR) colours and fainter absolute magnitude in the K-band when compared to their older spectral counterparts with higher field surface gravities (Gagné et al., 2015; Filippazzo et al., 2015). Liu et al. (2016) describes that J0835 appears to be redder than the bulk of low gravity BDs in the colour–magnitude diagram. They used the gravity-sensitive features (e.g. FeH, Na I, K I, and the H-band continuum shape) in its NIR SpeX prism spectrum (Burgasser et al., 2010) to classify J0835 as on the border between intermediate and field gravity. Their gravity classifications correspond to ages of, respectively, ~30–200 Myr and ~200 Myr. Sanghi et al. (2023) noted a lower surface gravity of $\log g = 4.32 \pm 0.24$, which may be related to their significantly different estimate of $T_{\rm eff}$.

The narrow CO features in the NIRSpec spectra of Blake et al. (2010) are indicative of it being a slow rotator (< 20 km s^{-1}). They forward-modelled the extracted spectra and found a rotational velocity of $v \sin i = 4.18 \pm 0.43$ km s^{-1}. With those values, Schlawin et al. (2017) provided an estimation of the inclination angle i of 21° (close to pole-on) from photometric variability monitoring, assuming a radius of one Jupiter radius.

L dwarfs often exhibit low-level, rotationally modulated photometric variability generally associated with heterogeneous, cloud-covered atmospheres. High-precision ground-based NIR spectrophotometry revealed its spectral variability, likely to be induced by the rapid 3.1 h rotation Koen et al. (2004). In contrast, Schlawin et al. (2017) observed a variability of less than 0.5% per band, with no clear spectral dependence, which is less variability than reported in previous work (Koen et al., 2004; Wilson et al., 2014). They use it to provide an estimation of the inclination angle i of 21° (close to pole-on), assuming a radius of 1 Jupiter radius.

2.2.2 J0501

2MASS J05012406-0010452, hereafter referred to as J0501, is a BD located in the constellation Orion (Reid et al., 2008). Cruz et al. (2009) classifies J0501 as a spectral type L4γ in the optical regime, after which both Liu et al. (2016) and Faherty et al. (2016) classify it as a young field object. Cruz et al. (2009) noted its unusual spectral features, such as notably weak FeH molecular absorption and weak Na I and K I doublets. From this, they concluded the object should have a low surface gravity and is likely a young, low-mass BD. Zapatero Osorio et al. (2014) estimated its effective temperature to be 1720 ± 55 K. Gagné et al. (2015) categorised J0501 in the IR as spectral type L3γ, providing evidence that J0501 is a member

of the Columba or Carina moving group (coeval at 20-40 Myr). In this case, the mass is estimated to be, $10.2^{+0.8}_{-1.0}$ M_{Jup} giving rise to a surface gravity of $\log g = 4.0 \pm 0.5$. Vos et al. (2020) measured a rotational velocity of $v \sin i = 9.57^{+0.67}_{-0.58}$ km s^{-1}, which in combination with a radius estimate (Filippazzo et al., 2015) results in a maximum rotation period of 15.7 ± 0.2 hr.

2.2.3 J0500

2MASS J05002100+0330501, from hereon referred to as J0500, is a BD at a distance of 13.23 ± 0.05 pc (Gaia Collaboration, 2020). Just like J0501, it is also located in the constellation Orion and part of the same moving group. Reid et al. (2008) characterised this BD as a spectral type L4. Filippazzo et al. (2015) estimated an effective temperature of 1793 ± 72 K and a surface gravity of $\log g = 5.2 \pm 0.19$ based on its bolometric luminosity. In addition, they derive a mass of 64 ± 14 M_{Jup} and a radius of 1.00 ± 0.08 R_{Jup}. Burningham et al. (2017) also estimated its effective temperature and surface gravity. They applied a spectral inversion technique in the cloudy L dwarf regime to obtain a temperature estimate of 1796^{+23}_{-25} K, a surface gravity of, $\log g = 5.21^{+0.05}_{-0.08}$ together with H_2O, CO, TiO, VO, CaH, CrH, FeH, Na, and K abundances. In comparison to thermochemical equilibrium abundances, they found that the CO and alkali abundances are a factor of ∼ 10 higher and ∼ 2 lower, respectively.

2.3 Observations and data reduction

2.3.1 Observations

The observations of J0835, J0501 and J0500, on January 2, February 2 and 28, 2023, respectively, were conducted as part of the SupJup Survey utilising CRIRES+ at the Very Large Telescope. CRIRES+ (Kaeufl et al., 2004; Dorn et al., 2014, 2023) is an advanced slit spectrograph with adaptive optics capabilities (Paufique et al., 2004), providing high resolution and able to target a broad wavelength range from 0.95 to 5.3 microns with a resolving power of up to $R \sim 100,000$. Our observations employed the K2166 wavelength setting (1.90 − 2.48 µm), focusing on regions featuring prominent ^{12}CO and ^{13}CO absorption lines. By utilising the wide slit mode, 0.4", a spectral resolution of $R \sim 64,000$, $R \sim 56,000$, and $R \sim 58000$ was obtained for the J0835, J0501, and J0500 observations, respectively (values calculated as described in Appendix A of González Picos et al. 2024). We were not able to use the adaptive optics system as the target BDs are too faint in the R-band used for wavefront sensing. Our observation sequence followed an ABBA nodding pattern, of 18, 12, and 4 individual exposures of 300 seconds for J0835, J0501, and J0500, respectively (see Table 2.2 for a complete overview of the observation parameters).

2.3.2 Data reduction

The data processing was conducted using the open-source package `excalibuhr` (Zhang et al., 2024). This involved various corrections including dark-subtraction, flat-fielding, bad-pixel masking and removal of sky emission via AB (or BA) pair subtraction. A and B nodding

position frames were mean-combined to produce master frames. After slit curvature and tilt adjustments, the optimal extraction algorithm (Horne, 1986) was applied to convert calibrated images into one-dimensional spectra. Telluric standard stars (see Table 2.2), observed with the same slit- and wavelength settings as the target observations and at similar airmasses, underwent the same reduction procedure.

Atmospheric corrections were performed using `Molecfit` (Smette et al., 2015). The standard star observations were used to fit the telluric model, which were subsequently scaled to the airmass and precipitable water vapour of the target observation (see González Picos et al. 2024). Detector pixels with telluric transmission of $< 70\%$ were masked in the observed spectra since they cannot be adequately corrected. The bluest of the seven spectral orders is heavily contaminated with tellurics and therefore not included in our analysis. In addition, the `Molecfit` model provides a secondary wavelength correction. Finally, the telluric-corrected spectra were flux-calibrated using a simple scaling factor derived from integrated flux measurements in the 2MASS Ks filter-curve and photometry data (Table 2.2).

2.4 Atmospheric modelling

We adopted a similar atmospheric retrieval framework as used in de Regt et al. (2024). We refer to their work for an elaborate description of the algorithm, likelihood and correlated noise. In this section we summarise the main principles.

2.4.1 Retrieval framework

The atmospheric retrieval framework is based on the radiative transfer code `petitRADTRANS` (`pRT`; Mollière et al., 2019), which computes emission spectra using descriptions of the atmospheric chemistry, cloud structure, surface gravity, and molecular or atomic opacities. `pRT` was integrated with the nested sampling tool `PyMultiNest` (Buchner et al., 2014), a Python interface for the `MultiNest` (Feroz et al., 2019) algorithm. All computations were executed in parallel on the Dutch National Supercomputer Snellius.

The model atmosphere was subdivided into a series of 50 layers covering the atmospheric vertical extent using a pressure range of $P = 10^2 - 10^{-5}$ bar. Each layer was characterised by a temperature and mass fractions of relevant chemical species. The radiative transfer equation was solved for each layer to obtain the flux as a function of wavelength.

Our models accounted for collision-induced absorption (Borysow et al., 1988) from H_2-H_2 and H_2-He (Dalgarno & Williams, 1962; Chan & Dalgarno, 1965; Gray, 2008), as well as Rayleigh scattering of H_2 and He. H_2O (or $H_2^{16}O$), ^{12}CO, ^{13}CO, hydrogen fluoride (HF), Ca and heavy-oxygen water ($H_2^{18}O$) were included as line opacities. We used ExoMol line lists for the opacities of heavy-oxygen water ($H_2^{18}O$; Polyansky et al. 2017) and $H_2^{16}O$ (Polyansky et al., 2018). The HITEMP (Rothman et al., 2010) line lists were employed for ^{12}CO, ^{13}CO (Li et al., 2015). Moreover, opacity from HF (Li et al., 2013; Coxon & Hajigeorgiou, 2015; Somogyi et al., 2021) was included as a line species following the detection of HF in the atmosphere of two young BDs (González Picos et al., 2024) and in YSES 1b (Zhang et al., 2024). Atomic opacity was included for Ca (Castelli & Kurucz, 2003) and several other atoms

were evaluated, but not included in the final model. Furthermore, no clouds were included in the atmospheric models (see section 2.4.3, for more details).

The pRT model spectra were Doppler-shifted to probe the object's radial velocity ($v_{\rm rad}$) and subsequently convolved with a rotational broadening kernel using the `fastRotBroad` routine (Gray, 2008) of `PyAstronomy`[1] (Czesla et al., 2019). The routine applies the projected rotational velocity ($v \sin i$) while taking into account the effects of limb-darkening, fitted with a linear limb-darkening coefficient ($\epsilon_{\rm limb}$). We implemented instrumental broadening, introduced by the slit spectrograph, by convolving the rotationally broadened spectra with a Gaussian kernel. The width of this kernel corresponds to the $R \sim 50.000$ spectral resolution of the CRIRES+ instrument. Lastly, the spectra are resampled to the observed wavelength grid for direct comparison with the data.

Generating the significant number of pRT model spectra needed for a statistically supported retrieval is time expensive. The computations of the pRT spectra were sped up by under-sampling the high-resolution ($\lambda/\Delta\lambda = 10^6$) line-by-line opacities (implemented by setting `lbl_opacity_sampling= 3`, i.e. $R \sim 10^6/3$). The work, done by de Regt et al. (2024) and González Picos et al. (2024), demonstrates that this degree of undersampling is appropriate given the CRIRES+ spectral resolution.

The sampling tool `PyMultiNest` builds up posterior distributions by sampling the parameter-space of the 18 free parameters and evaluating the likelihood function between the observed and pRT spectra, while obtaining Bayesian evidence (Z) estimates simultaneously. This is an efficient method for exploring and sampling from complex, high-dimensional parameter spaces. A constant sampling efficiency of 5% was used in the importance nested sampling mode. Following Feroz et al. (2019), González Picos et al. (2024), and de Regt et al. (2024), we used 400 live points and an evidence tolerance of 0.5 to sample the posterior distributions. The priors of the retrieved parameters can be found in Table 2.3.

2.4.2 Likelihood and correlated noise

We adopted the same likelihood function as used in Landman et al. (2024), González Picos et al. (2024), and de Regt et al. (2024), which is based on the formalism defined by Ruffio et al. (2019). For 18 order-detector pairs (6 spectral orders covered by 3 detectors each), the log-likelihood ($\ln \mathcal{L}$) is calculated as

$$\ln \mathcal{L} = -\frac{1}{2}\left(N \ln(2\pi) + \ln\left(|\boldsymbol{\Sigma}_0|\right) + N \ln\left(s^2\right) + \frac{1}{s^2}\boldsymbol{R}^T \boldsymbol{\Sigma}_0^{-1} \boldsymbol{R}\right), \tag{2.1}$$

where N is the number of unmasked pixels (2048 at most), s is the uncertainty scaling factor for the total covariance matrix $\boldsymbol{\Sigma}_0$ and $\boldsymbol{R} = \boldsymbol{d} - \phi\boldsymbol{m}$ represents the residuals between the observed ($\boldsymbol{d}$) and model ($\boldsymbol{m}$) spectra for each order-detector pair. The optimal solution for the flux-scaling parameter $\tilde{\phi}$ and the optimally scaled residuals $\tilde{s}^2$, are found by calculating

$$\tilde{\phi} = (\boldsymbol{m}^T \Sigma_0^{-1} \boldsymbol{m})^{-1} \boldsymbol{m}^T \Sigma_0^{-1} \boldsymbol{d}, \qquad \text{and} \quad \tilde{s}^2 = \frac{1}{N} \boldsymbol{R}^T \boldsymbol{\Sigma}_0^{-1} \boldsymbol{R}\Big|_{\phi=\tilde{\phi}}. \tag{2.2}$$

[1] https://github.com/sczesla/PyAstronomy

de Regt et al. (2024) highlighted the importance of accounting for correlated noise in CRIRES+ spectra when retrieving model parameter solutions. Using Gaussian processes (GPs), we made sure to model the correlated noise (Kawahara et al., 2022), and address the problem of biases in the retrieved parameters and underestimation of their uncertainties. The covariance of pixels i and j are calculated by adding a diagonal, uncorrelated variance term and an off-diagonal correlated uncertainty term to achieve

$$\Sigma_{0,ij} = \delta_{ij}\sigma_i^2 + a^2\sigma_{\mathrm{eff},ij}^2 \exp\left(-\frac{r_{ij}^2}{2\ell^2}\right). \tag{2.3}$$

In Eq. 2.3, δ_{ij} is the Kronecker delta function, σ_i the flux uncertainty of pixel i, $\sigma_{\mathrm{eff},ij}$ the effective uncertainty derived from the data arithmetic mean of the variances of pixels i and j, r_{ij} the wavelength separation between pixels, and a and ℓ the GP amplitude and length scale, respectively. The GP amplitude and length scale are retrieved as free parameters.

2.4.3 Pressure–temperature profile

In general, BDs are self-luminous objects devoid of significant external irradiation. In the atmosphere, where convection dominates, the atmospheres are expected to have a pressure–temperature (P–T) profile in an adiabatic form (Baraffe et al., 2002; Ludwig et al., 2006; Freytag et al., 2010), which implies that both the atmospheric pressure and temperature increase with the atmospheric depth.

The atmospheres were modelled using a similar parametrisation as presented in Zhang et al. (2023). The temperature was parametrised as a function of pressure using values for the temperature gradient $\nabla T_i \equiv \frac{d\ln T_i}{d\ln P_i}$, where, i corresponds to the number of pressure knots in log-space. In our retrievals, we used five pressure knots where the higher and lower knots are fixed ($P_1 = 10^2$ and $P_5 = 10^{-5}$). The three intermediate knots were allowed to shift their values. This approach prevented a biased location of the photosphere (see González Picos et al. (2024)).

The temperature gradients, ∇T_j, of each atmospheric layer were calculated using linear interpolation of the temperatures associated with the pressure knots. Thereafter, the temperatures of each layer were determined using

$$T_j = T_{j-1}\left(\frac{P_j}{P_{j-1}}\right)^{\nabla T_j}. \tag{2.4}$$

The central knot ($i = 3$) was set to be an anchor point for the temperature. As a result, for each model, we retrieved five temperature gradients, three pressure points, and the temperature at the central knot.

We investigated the presence of clouds in the atmospheres of our targets. We made no assumptions regarding cloud composition, and we parametrised the clouds using a 'grey' continuum opacity applied at all wavelength. Clouds are likely to have an effect on the strength of the overall continuum and the shape of the temperature profile. No evidence of the presence of clouds was found and therefore clouds were excluded from the final retrieval analyses. This does not mean that these are cloudless objects. They may be present below the K-band

photosphere, or equally modelled with a more isothermal P-T profile with similar values for $T_{\rm eff}$, $\log g$ and chemical abundances (Mollière et al., 2020; Zhang et al., 2023). Various retrieval studies of high-resolution K-band spectra resulted in cloud-free solutions as well (e.g. Zhang et al., 2021; Landman et al., 2024), where Landman et al. (2024) compared models with various and without clouds revealing a consistent C/O abundance ratio. Combining the K-band observations with short-wavelength observations (e.g. Y- or J-band), combining extensive BD photometry measurements with a wider wavelength range, or using the silicate features around 8 – 10 μm (Miles et al., 2023), may further constrain the cloud properties (de Regt et al., 2024).

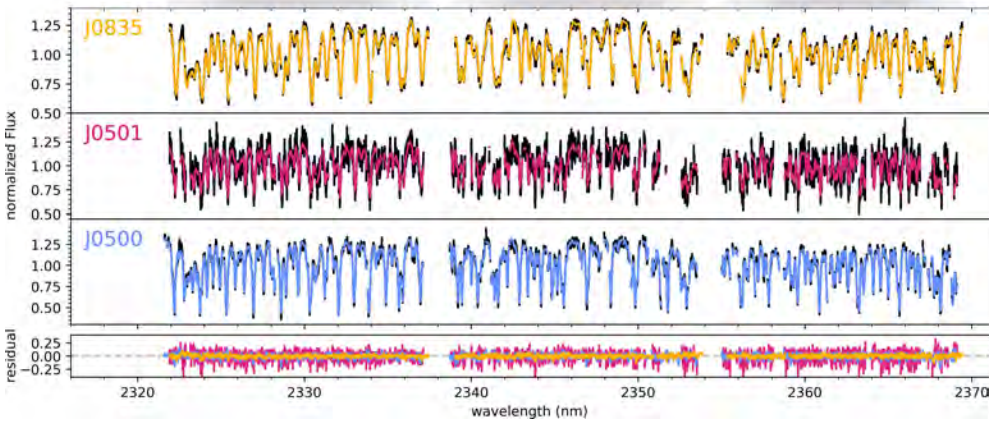

Figure 2.2: Best-fitting models retrieved for J0835, J0501 and J0500 (top to bottom). The upper three panels show the observational flux in black, and the best-fitting model spectra for the three BDs. The observed flux is normalised to the mean flux of each order–detector pair after telluric correction. The lower panel shows the residuals between the observed and model spectra. The data and the models are displayed in the rest frame of each object. The shaded region at the top of the image indicates the wavelength coverage of the three detectors for each spectral order (CRIRES+ and K2166 wavelength setting). They slightly differ in the rest-frame of the BDs as presented by the gradient. The sixth order (2321.6 – 2369.6 nm) is shown because it contains several ^{12}CO and ^{13}CO lines. The data and best-fitting models of the remaining orders can be found in Appendix 2.B.

2.4.4 Chemical Composition

A free-chemistry approach (de Regt et al., 2024) was adopted in which the mixing ratios of line species were treated as independent parameters. This method, also referred to as the free composition (FC) method, includes vertically constant abundances of relevant chemical species while not enforcing any constraints on the relative abundances. The He abundance is held constant at $n_{\rm He} = 0.15$ and the H_2 abundance is adjusted to obtain a total $n_{\rm tot}$ equal to unity. The constant-with-altitude mixing ratios are expected to be valid for most scenarios for our K-band spectra, as only a limited vertical extent of the BD atmospheres is probed.

The C/O ratios are determined using the chemical abundances of carbon n_C and oxygen n_O bearing species, according to

$$C/O = \frac{n_{^{12}CO} + n_{^{13}CO}}{n_{H_2O} + n_{^{12}CO} + n_{^{13}CO}}. \tag{2.5}$$

The C/O ratio is constant, due to the constant-with-altitude mixing ratios.

The carbon abundance relative to hydrogen is used as a measurement of metallicity:

$$[C/H] = \log_{10}\left(\frac{n_C}{n_H}\right) - \log_{10}\left(\frac{n_C}{n_H}\right)_\odot, \tag{2.6}$$

where the solar value is $\log_{10}\left(\frac{n_C}{n_H}\right)_\odot = -3.54 \pm 0.04$ (Asplund et al. (2021). In a similar manner, the fluorine abundance from HF is calculated through

$$[F/H] = \log_{10}\left(\frac{n_{HF}}{n_H}\right) - \log_{10}\left(\frac{n_{HF}}{n_H}\right)_\odot, \tag{2.7}$$

where the solar value is $\log_{10}\left(\frac{n_F}{n_H}\right)_\odot = -7.6 \pm 0.25$ (Asplund et al. (2021).

We independently retrieved the number fractions of ^{12}CO, ^{13}CO, $H_2^{16}O$, and $H_2^{18}O$ to determine the carbon and oxygen isotopologue ratios ($^{12}C/^{13}C$ and $^{16}O/^{18}O$, respectively) of our BD sample. We want to compare our values of the retrieved carbon and oxygen isotope ratios with those of González Picos et al. (2024). We calculated these ratios using

$$^{12}C/^{13}C = \frac{n_{^{12}CO}}{n_{^{13}CO}}; \qquad ^{16}O/^{18}O = \frac{n_{H_2^{16}O}}{n_{H_2^{18}O}}. \tag{2.8}$$

To ensure the reliability of detecting molecular species, we employ a cross-correlation analysis, as detailed in Zhang et al. (2021). The cross-correlation function (CCF) for each species, X, is computed as follows:

$$CCF_X(v) = \sum_{i=1}^{N_\lambda} \frac{\left(d_i - m_{i,\bar{X}}\right)\left(m_i - m_{i,\bar{X}}\right)}{\sigma_i^2}, \tag{2.9}$$

where $m_{i,\bar{X}}$ is the atmospheric model without the species X, and m_i is the model with all species included in the retrieval.

2.5 Results & Discussion

This section summarises the main results regarding the chemical composition, thermal profile, surface gravity, and rotational velocity of the three BDs, and provides a comparison between free and equilibrium chemistry (EC) models.

All results were obtained by analysing the atmospheric retrievals run for J0835, J0501 and J0500. Our best-fitting spectral models resulting from the retrieval analysis are shown

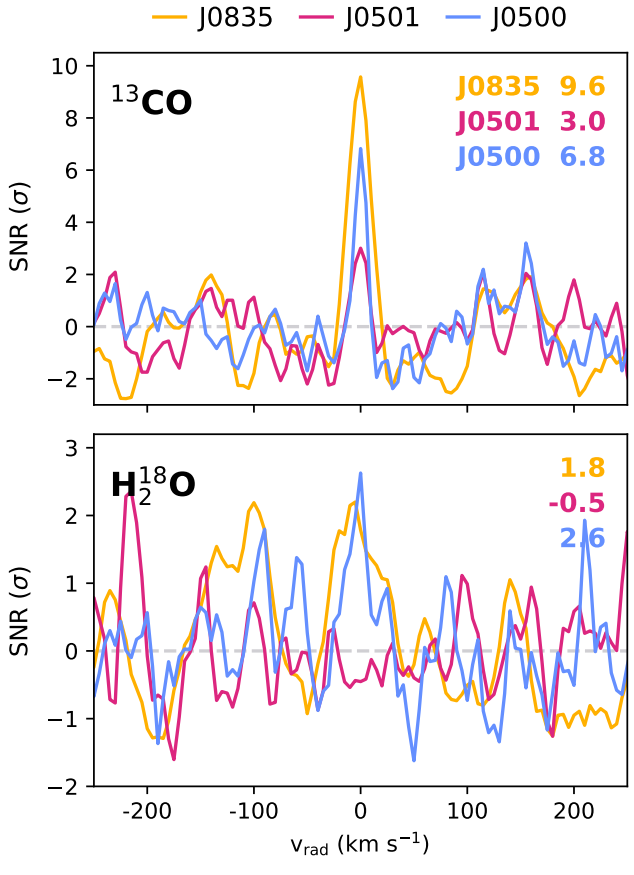

Figure 2.3: CCFs for ^{13}CO and $H_2^{18}O$. The CCFs were calculated for each order–detector pair and summed over all orders and detectors, after which they were converted to S/N by dividing by the standard deviation of the CCFs away from the peak, excluding the values within $-100 < v_{rad} < 100$ km s^{-1}. The different colours represent the different targets, J0835, J0501 and J0500. The S/Ns of the peaks of the CCFs for each individual species are shown in the upper-right corner.

in the top three panels of Fig. 2.2. These models implement a free-chemistry atmosphere and account for pixel-to-pixel correlation using GPs (de Regt et al., 2024; González Picos et al., 2024). The detection significances (X) of four species (^{13}CO, $H_2^{18}O$, HF, and Ca) were determined from a Bayesian model comparison. This included running 15 retrievals, five retrievals for every BD, one model including all X and the main species (^{12}CO, $H_2^{16}O$), and four models where one X was excluded. We computed the logarithm of the Bayes factor B_m according to

$$\ln B_m = \ln \mathcal{Z}_{\text{full model}} - \ln \mathcal{Z}_{\text{w/o } X}, \tag{2.10}$$

where $\ln \mathcal{Z}$ stands for the log-evidence calculated for every retrieval. Thereafter, this is translated to a detection significance, also referred to as the 'sigma' significance, in units of σ (Benneke & Seager, 2013). For ^{13}CO, we report moderate to strong detections of 9.6σ, 3.0σ, and 6.8σ for J0835, J0501, and J0500, respectively, see Figure 2.3. For $H_2^{18}O$ only one weak detection (2.6σ) for J0835 was found. All other BDs did not show any evidence of the presence of $H_2^{18}O$. This is the same case for Ca, with one weak detection (2.1σ) for J0500. All BDs show a strong detection significance for HF ($> 4.0\sigma$). An overview of all B_m and sigma significance values is presented in Appendix A.

We calculated the CCF using Eq. 2.9 between the data and the best-fit model of each individual species for every order-detector pair in the object rest frame. These CCFs are then combined across all orders and detectors and converted to signal-to-noise ratios (S/Ns) [σ] by dividing by the standard deviation of the CCFs away from the peak, excluding the values within $-100 < v_{\text{rad}} < 100$ km s^{-1}. The resultant S/Ns distinctly show the presence of various species in the BD atmospheres (see Appendix 2.C).

The three objects generally show comparable chemical compositions and temperature distributions. However, variations are noted due to differences in their effective temperatures, surface gravities, rotational velocities, and the quality of the observational data. Table 2.3 provides an overview of the retrieved parameters for all three best-fitting spectral models, with their prior values. All uncertainties indicate 1σ intervals.

2.5.1 Chemical Composition

Our best-fitting spectral models yield the volume mixing ratios (VMRs) of detectable species (see Table 2.3) in the atmospheres of the three BDs. Constraints are obtained for both H_2O and CO for all three targets, leading to a gaseous C and O inventory and subsequent C/O ratio, metallicity, and isotope ratios of the targets. In addition, we present the fluorine abundance for all three BDs.

C/O ratio

The C/O ratio posteriors are shown in Fig. 2.4, which presents the retrieved values:

$$\begin{aligned} \text{C/O}_{\text{J0835}} &= 0.65^{+0.02}_{-0.02} \\ \text{C/O}_{\text{J0501}} &= 0.68^{+0.04}_{-0.04} \\ \text{C/O}_{\text{J0500}} &= 0.71^{+0.01}_{-0.01}. \end{aligned}$$

Parameter	Description	Prior Range	J0835	J0501	J0500
log ^{12}CO	log mixing ratio of ^{12}CO	[-12.0, -2.0]	$-2.85^{+0.02}_{-0.02}$	$-2.89^{+0.05}_{-0.05}$	$-3.03^{+0.02}_{-0.02}$
log ^{13}CO	log mixing ratio of ^{13}CO	[-12.0, -2.0]	$-4.80^{+0.05}_{-0.05}$	$-5.06^{+0.14}_{-0.15}$	$-5.10^{+0.06}_{-0.07}$
log $H_2^{16}O$	log mixing ratio of $H_2^{16}O$	[-12.0, -2.0]	$-3.23^{+0.02}_{-0.02}$	$-3.19^{+0.05}_{-0.05}$	$-3.29^{+0.02}_{-0.02}$
log $H_2^{18}O$	log mixing ratio of $H_2^{18}O$	[-12.0, -2.0]	$-5.73^{+0.12}_{-0.16}$	$-8.92^{+1.96}_{-1.99}$	$-5.69^{+0.13}_{-0.21}$
log HF	log mixing ratio of HF	[-12.0, -2.0]	$-7.03^{+0.05}_{-0.05}$	$-7.10^{+0.19}_{-0.19}$	$-7.30^{+0.06}_{-0.06}$
log Ca	log mixing ratio of Ca	[-12.0, -2.0]	$-6.03^{+0.22}_{-0.64}$	$-5.86^{+0.40}_{-1.38}$	$-5.95^{+0.14}_{-0.18}$
C/O	carbon-to-oxygen ratio	—	$0.65^{+0.02}_{-0.02}$	$0.68^{+0.04}_{-0.04}$	$0.71^{+0.01}_{-0.01}$
^{12}C/^{13}C	carbon isotope ratio	—	89^{+11}_{-11}	155^{+56}_{53}	117^{+20}_{-17}
^{16}O/^{18}O	oxygen isotope ratio	—	316^{+117}_{-89}	—	251^{+122}_{-76}
[F/H]	fluorine abundance w.r.t. solar	—	$0.41^{+0.05}_{-0.05}$	$0.26^{+0.19}_{-0.19}$	$0.07^{+0.06}_{-0.06}$
[C/H]	metallicity w.r.t. solar	—	$0.54^{+0.04}_{-0.04}$	$0.44^{+0.06}_{-0.06}$	$0.28^{+0.04}_{-0.04}$
log g	log surface gravity (cm s^{-2})	[4.00, 6.00]	$5.40^{+0.03}_{-0.03}$	$4.51^{+0.07}_{-0.07}$	$5.55^{+0.03}_{-0.03}$
$\epsilon_{\rm limb}$	limb darkening coefficient	[0.00, 1.00]	$0.63^{+0.06}_{-0.07}$	$0.37^{+0.28}_{-0.22}$	$0.31^{+0.24}_{-0.20}$
$v \sin i$	projected rotational velocity (km s^{-1})	[0.0, 40.0]	$15.42^{+0.14}_{-0.12}$	$6.90^{+0.25}_{-0.24}$	$5.05^{+0.21}_{-0.16}$
$v_{\rm rad}$	radial velocity (km s^{-1})	[-50.0, 50.0]	$29.59^{+0.04}_{-0.04}$	$23.15^{+0.05}_{-0.05}$	$15.65^{+0.02}_{-0.02}$
$\nabla_{T,0}$	temperature gradient at $P_0 = 10^2$ bar	[0.12, 0.40]	$0.15^{+0.03}_{-0.02}$	$0.15^{+0.09}_{-0.09}$	$0.22^{+0.06}_{-0.06}$
$\nabla_{T,1}$	temperature gradient at P_1	[0.13, 0.40]	$0.13^{+0.00}_{-0.00}$	$0.14^{+0.06}_{-0.06}$	$0.15^{+0.01}_{-0.01}$
$\nabla_{T,2}$	temperature gradient at P_2	[0.03, 0.40]	$0.06^{+0.00}_{-0.00}$	$0.10^{+0.02}_{-0.02}$	$0.09^{+0.01}_{-0.01}$
$\nabla_{T,3}$	temperature gradient at P_3	[0.00, 0.40]	$0.26^{+0.07}_{-0.06}$	$0.05^{+0.01}_{-0.01}$	$0.09^{+0.02}_{-0.01}$
$\nabla_{T,4}$	temperature gradient at $P_4 = 10^{-5}$ bar	[-0.20, 0.20]	$0.01^{+0.12}_{-0.13}$	$0.07^{+0.02}_{-0.03}$	$0.01^{+0.11}_{-0.12}$
log P_3	log pressure of central ($i = 3$) knot	[-3, 1]	$-0.30^{+0.08}_{-0.06}$	$0.66^{+0.19}_{-0.22}$	$0.12^{+0.18}_{-0.18}$
$\Delta \log P_{23}$	log pressure difference P_2 and P_3	[0.5, 2.0]	$1.66^{+0.22}_{-0.30}$	$1.40^{+0.08}_{-0.09}$	$1.46^{+0.34}_{-0.40}$
$\Delta \log P_{34}$	log pressure difference P_3 and P_4	[0.5, 1.0]	$0.93^{+0.05}_{-0.06}$	$0.69^{+0.06}_{-0.06}$	$0.81^{+0.11}_{-0.14}$
T_3	temperature at central ($i = 3$) knot (K)	[500, 2500]	1566^{+16}_{-13}	1977^{+85}_{-92}	1570^{+69}_{-59}
log a	GP amplitude	[-0.70, 0.30]	$-0.01^{+0.01}_{-0.01}$	$0.07^{+0.01}_{-0.01}$	$0.12^{+0.00}_{-0.00}$
log ℓ	GP length scale nm)	[-3.00, -1.00]	$-1.32^{+0.02}_{-0.02}$	$-2.06^{+0.01}_{-0.01}$	$-1.58^{+0.01}_{-0.01}$

Table 2.3: Retrieved best-fit parameters and their 1σ uncertainty intervals: We imposed uniform priors. The table includes the VMRs of the chemical species, physical properties (surface gravity and projected rotational velocity), temperature gradients and GP parameters.

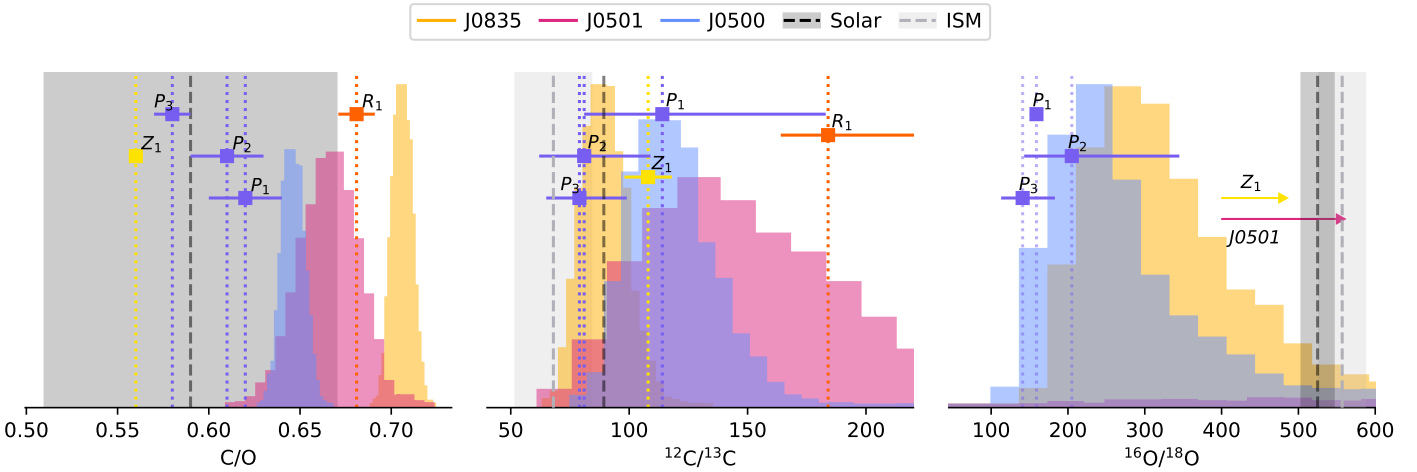

Figure 2.4: Posterior distributions of the C/O (left), carbon $^{12}C/^{13}C$ isotope (middle), and oxygen $^{16}O/^{18}O$ isotope ratio (right) for J0835, J0501 and J0500. The $^{12}C/^{13}C$ values for the Solar System (terrestrial value) and ISM are 89.3 ± 0.2 (Meija et al., 2016) and 68 ± 16 (Milam et al., 2005), respectively. The C/O value for our Sun is 0.59 ± 0.08 (Asplund et al., 2021). The $^{16}O/^{18}O$ values for the Solar System and ISM are 557 ± 30 (Wilson, 1999) and 525 ± 21 (Lyons et al., 2018). The purple error bars represent the young BDs observed and analysed by González Picos et al. (2024, P_1: J1200, P_2: TWA28 and P_3: J0856), the orange error bar DENIS J0255 (R_1) by de Regt et al. (2024), and the yellow 2M0355 (Z_1) by Zhang et al. (2022).

The C/O ratios are comparable among the three BDs, but slightly enhanced compared to the solar C/O ratio (0.59 ± 0.08, Asplund et al. (2021)). This enhancement may be explained by oxygen sequestration, (Line et al., 2021) leading to the condensation of oxygen into silicate-oxide clouds. This scenario was brought up by (de Regt et al., 2024) to explain the increased C/O ratio of ∼0.68 of BD DENIS J0255.

In Fig. 2.4, we compare the retrieved values for the three BDs to the values of other isolated BDs. The C/O ratios retrieved by González Picos et al. (2024) for three young late M-type BDs were within the margins of the solar ratio. In comparison, González Picos et al. (2024) studied M-type objects that have high enough atmospheric temperatures that silicate-oxide clouds do not form, thus explaining their agreement with the solar value. For 2M0355, Zhang et al. (2021) obtained a C/O ratio using an EC model that accounts for condensation. As such, their C/O ratio, which is in agreement with the solar ratio, represents the bulk elemental abundances.

Using the same EC set-up as de Regt et al. (2024), we find bulk C/O ratios of $0.58^{+0.01}_{-0.01}$, $0.60^{+0.02}_{-0.05}$, and $0.60^{+0.01}_{-0.01}$ for J0835, J0501, and J0500, respectively. They are in agreement with the solar C/O ratio.

Metallicity

The [C/H] ratio is used as a proxy for metallicity. The derived posterior distributions of [C/H] are shown in the bottom graph of Fig. 2.5. The [C/H] values are significantly larger than the solar value and other work that used this same proxy (Zhang et al., 2022; González Picos et al., 2024; de Regt et al., 2024). It is unfortunately not straightforward to interpret these values, since metallicities cannot be constrained well with solely K-band high-resolution spectroscopy because of the strong correlation between surface gravity and metallicity in atmospheric retrieval analyses (e.g. González Picos et al., 2024).

Isotope ratios

Constrained ^{12}CO and ^{13}CO abundances were retrieved for all three BDs. From those, the following ^{12}C/^{13}C ratios for J0835, J0501, and J0500 were determined (see Fig. 2.4):

$$
\begin{aligned}
^{12}\mathrm{C}/^{13}\mathrm{C}_{\mathrm{J0835}} &= 89^{+11}_{-11} \\
^{12}\mathrm{C}/^{13}\mathrm{C}_{\mathrm{J0501}} &= 155^{+56}_{-53} \\
^{12}\mathrm{C}/^{13}\mathrm{C}_{\mathrm{J0500}} &= 117^{+20}_{-17}.
\end{aligned}
$$

The values are similar among the three objects within their 1σ uncertainties. The ratio for J0835 is in agreement with the solar value of 89.3 ± 0.2 (Meija et al., 2016), while the other two objects appear to have slightly larger ratios. All three of them have significantly higher ratios than the present day ISM value 68 ± 16 (Milam et al., 2005). Figure 2.4 gives an overview of our retrieved ratios in comparison to previous work as part of the SupJup Survey (González Picos et al., 2024; de Regt et al., 2024), and the work on BD 2M0355, the first BD for which the ^{12}C/^{13}C was determined (Zhang et al., 2021; Zhang et al., 2022).

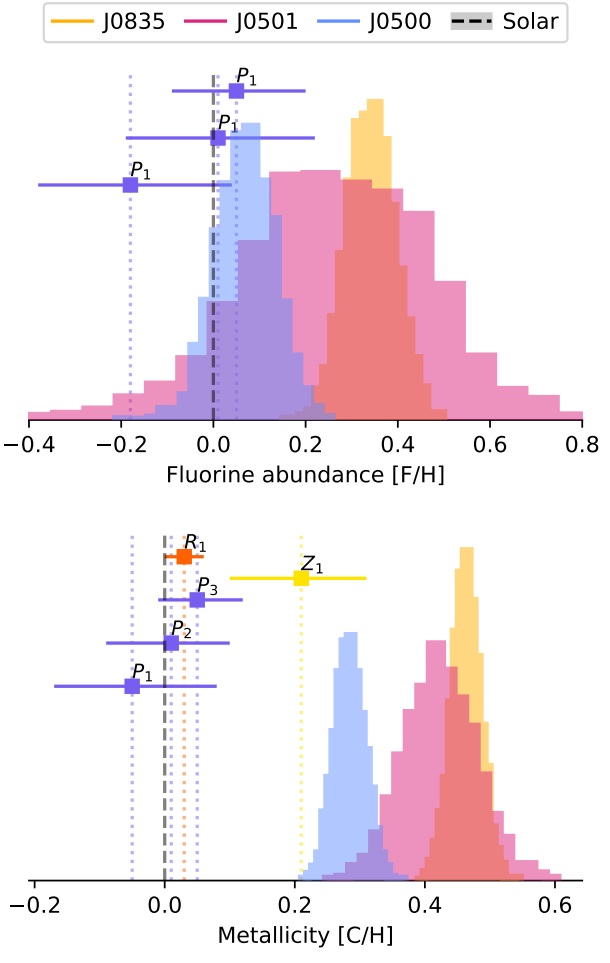

Figure 2.5: Posterior distributions of the fluorine abundance relative to hydrogen [F/H] (**top panel**) and carbon abundance relative to hydrogen [C/H], used as a measure of metallicity (**bottom panel**) for J0835, J0501 and J0500. J1200, TWA28, and J0856 are the young BDs observed and analysed by González Picos et al. (2024), DENIS by de Regt et al. (2024), and 2M0355 by Zhang et al. (2022). $\log_{10}[\mathrm{F/H}]_\odot = -7.6 \pm 0.25$ (Asplund et al. (2021)) and $\log_{10}[\mathrm{C/H}]_\odot = -3.54 \pm 0.04$ (Asplund et al. (2021)).

The $H_2^{18}O$ isotope was included in the retrievals because of the positive detection of $H_2^{18}O$ by González Picos et al. (2024) in TWA 28 ($^{16}O/^{18}O \sim 205^{+140}_{-62}$) and J0856 ($^{16}O/^{18}O \sim 141^{+42}_{-28}$). As mentioned before, only one weak detection was found for J0835. From these retrieved VMRs, we calculated the $^{16}O/^{18}O$ ratio for J0835:

$$^{16}O/^{18}O_{J0835} = 311^{+100}_{-86}.$$

Zhang et al. (2021) and Line et al. (2021) have highlighted the potential of the carbon isotope ratio to serve as an additional diagnostic of planet and BD formation histories. However, evolution on a galactic timescale is also expected to alter the average $^{12}C/^{13}C$ ratio, since ^{13}C is produced in asymptotic giant branch stars that subsequently enrich the ISM (Iben & Renzini, 1983). Therefore, young objects are generally expected to have lower ratios than old objects. Crossfield et al. (2019) found isotopologue ratio measurements for GJ 745 A and B of $^{12}C/^{13}C = 296 \pm 45$ and 224 ± 26, and $^{16}O/^{18}O = 1220 \pm 260$ and 1550 ± 360, respectively. Caramazza, M. et al. (2023) suggested, after observing the X-ray emission for GJ 745 A and B, that the extremely low X-ray activity of the binary, their ultra-low metallicity, non-detection of photometric star spot variability, and low chromospheric emission are in line with an older age object. As far as we know, these are the highest carbon and oxygen isotope ratios measured for mature low-mass stars.

Hydrogen fluoride

The abundances of fluorine (F) with respect to solar were computed from the retrieved VMRs of HF:

$$[\mathrm{F/H}]_{\mathrm{J0835}} = 0.41^{+0.05}_{-0.05}$$
$$[\mathrm{F/H}]_{\mathrm{J0501}} = 0.26^{+0.19}_{-0.19}$$
$$[\mathrm{F/H}]_{\mathrm{J0500}} = 0.07^{+0.06}_{-0.06}.$$

All BDs show a strong HF detection significance: 14.5σ, 4.2σ, and 9.2σ for J0835, J0501, and J0500, respectively.

The computed [F/H] ratio for J0500 is in a 1σ agreement with the solar abundance of $\log_{10}\left(\frac{n_{\mathrm{F}}}{n_{\mathrm{H}}}\right)_{\odot} = -7.6 \pm 0.25$ (Asplund et al., 2009), J0501 is in agreement within 2σ, and J0835 shows a higher value for [F/H]. It should be noted that the [F/H] suffers from the same metallicity-surface gravity degeneracy as the [C/H] and thus the absolute fluorine abundance of J0835 is not necessarily super-solar.

For our K-band observations, we are sensitive to the HF $1-0$ vibrational transitions, as it has prominent absorption lines in the $2.3-2.5$ µm region (Wilzewski et al., 2016). Recent work in the SupJup Survey, operating in the K-band, has revealed the presence of HF in several sub-stellar objects (González Picos et al., 2024; Zhang et al., 2024; de Regt et al., 2025). Figure 2.5 gives an overview of all values obtained so far.

2.5.2 Free chemistry versus equilibrium chemistry

As elaborated in section 2.4.4, the FC method (e.g. de Regt et al., 2024; González Picos et al., 2024) was applied. This method assumes a constant-with-altitude mixing ratio for every species in the model atmospheres. Despite the FC method providing a good approximation for our spectra, it is insightful to compare our retrieved abundances against those predicted by EC. The EC method assumed element abundances as retrieved from the `pRT` models (see Fig. 2.6).

Using `FastChem` (Stock et al., 2018, 2022; Kitzmann et al., 2024) we compared our retrieved mixing ratios against EC predictions (see Fig. 2.6). The VMRs are normalised

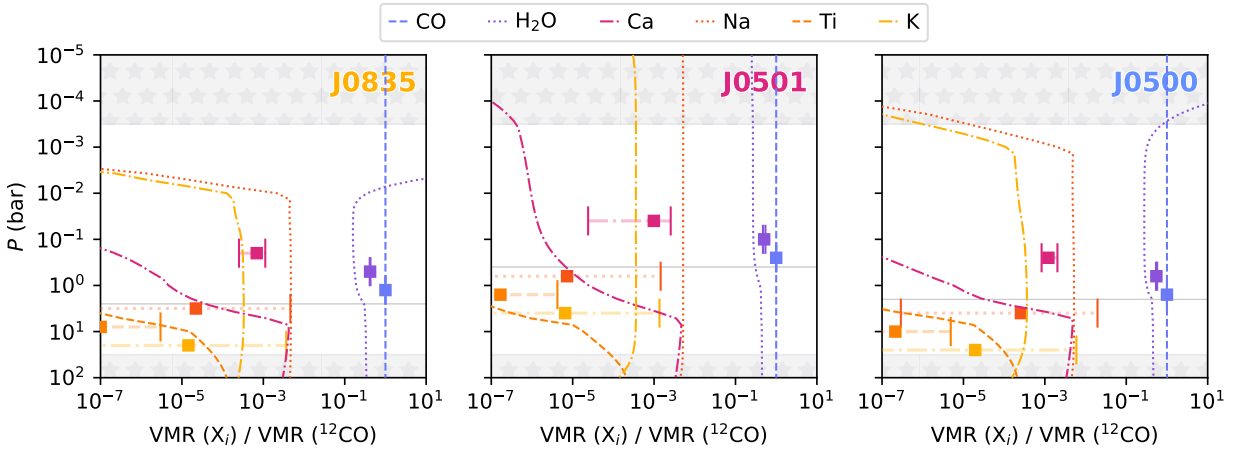

Figure 2.6: VMRs of line species (^{12}CO, H_2O, Ca, Na, Ti, and K) for the three BDs using the FC and EC method. The error bars represent the values retrieved with the FC method. The dashed lines show the `Fastchem` EC abundances corresponding to the best-fitting P-T profile, C/O ratio, and metallicity for each of the BDs. The EC abundances have a similar line style and colour as those of the associated FC VMR. The black lines indicate the location of the peak of the integrated contribution functions, and the shaded areas indicate the pressures where we expect large uncertainties as we are not sensitive to probe these atmospheric pressures.

relative to the VMR of ^{12}CO, which corrects for any potential systematic offsets due to the metallicity-surface gravity degeneracy (González Picos et al., 2024; de Regt et al., 2024). The H_2O abundance retrieved with the FC method deviates slightly from the EC predictions, which could indicate the presence of quenching and/or disequilibrium chemistry.

Besides the line species presented in Table 2.3 various `pRT` models including the atomic species Na, Ti and K were tested against the spectra. The Na and K, or alkali lines, have been found to be a very good probe for differences in surface gravity for late-type objects (Gorlova et al., 2003; Schlieder et al., 2012; Allers & Liu, 2013; Martin et al., 2017; Manjavacas et al., 2020). For young BDs, alkali lines have been observed to be weaker than for field BDs (Steele & Jameson, 1995; Gorlova et al., 2003; Allers et al., 2007; Allers & Liu, 2013; Bonnefoy et al., 2014).

The atomic opacities from Na, K (Allard et al., 2019), and Ti (Castelli & Kurucz, 2003) were included in our FC retrievals, but not detected. The retrieved abundances using the FC models are displayed by the error bars in Fig. 2.6. The dashed lines represent those for the EC models. Indeed, the derived VMR upper limits for Na, Ti, and K are in line with those expected from the EC models.

The H_2O, Na and K EC abundances of J0835 and J0500 are skewed for smaller pressures. For lower temperatures, CH_4 becomes the dominating carbon species, yielding a drop-off for the CO abundances. The increase in the relative H_2O abundances is expected since the models are normalised towards CO. We retrieved a lower temperature in the upper atmosphere of J0835 than J0500, which explains the drop-off location for J0835 to be at a higher pressure. For J0501, the temperature does not get low enough to see this CO-CH_4 switch. Even though we retrieve these abundances, the presence of a similar shift is unlikely due to the vertical mixing in the atmospheres (Zahnle & Marley, 2014).

2.5.3 Thermal Profile

The best-fitting P-T profiles (the solid line and the shaded areas indicate the 1σ, 2σ, and 3σ uncertainties in Fig. 2.7) of the BDs J0835 and J0500 are similar, while the profile of J0501 is warmer by ~100 K at similar pressures. Since the retrieved surface gravity of J0501 is lower than that of the others by an order of magnitude, the photospheric region, as indicated by the integrated contribution function (shaded area on the left in Fig. 2.7), is found to be located at lower pressures (order of ~10). This is in line with the mass and radii estimates for the three targets by Filippazzo et al. (2015), where J0501 is found to be of significantly lower mass and larger radius. As expected, the confidence envelopes of the P-T profile show larger uncertainties outside the photosphere, at the higher and lower altitudes. These regions are not probed by the K-band spectrum.

The self-consistent Sonora elf owl models (SE_1 and SE_2 in Fig. 2.7) were calculated using T_{eff} = 1800 K and $\log g = 5.5$, and T_{eff} = 1700 K and $\log g = 4.5$, both assuming a solar metallicity and C/O ratio. Just as found for YSES 1b (Zhang et al., 2024), the retrieved P-T profiles are more isothermal than the self-consistent models. This may indicate the absence of continuum opacity, for example clouds, since a spectrum of a cloudless atmosphere combined with an isothermal temperature gradient is equivalent to a spectrum of a cloudy atmosphere.

To a first order, the retrieved thermal profiles for all three objects seem to agree well

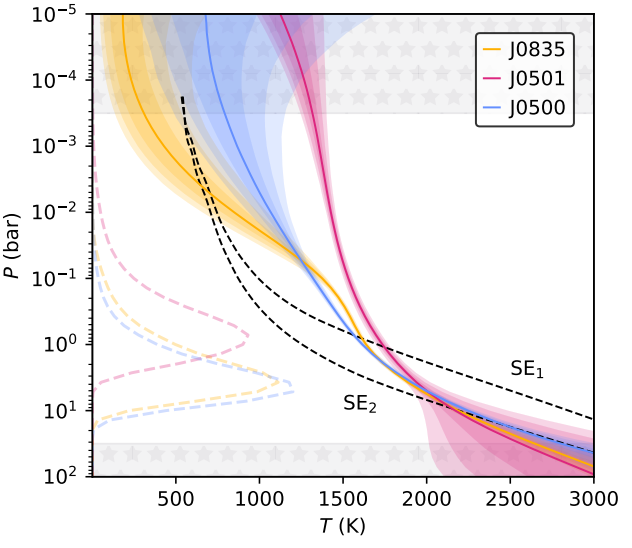

Figure 2.7: Best-fit P–T profiles (solid lines) for BDs J0835, J0501 and J0500. The associated shaded regions indicate the 1σ, 2σ, and 3σ regions. The integrated contribution functions are indicated on the left vertical axis. Two self-consistent Sonora elf owl P-T profiles, SE_1 (T_{eff} = 1800 K, $\log g = 5.5$) and SE_2 (T_{eff} = 1700 K, $\log g = 4.5$) are over-plotted with dashed black lines.

with the literature values for the effective temperature of each object (see Table 2.1). A direct comparison of our profiles to the literature values is unfavourable, due to the disparate methods used to derive the literature values.

2.5.4 Surface gravity

The retrieved values for the surface gravity, $\log g$, are in line with the expectations for young, low-surface gravity objects (Baraffe et al., 2002; Allers et al., 2007; Bonnefoy et al., 2014). While the surface gravity values for J0835 and J0500 are similar, J0501 shows a significantly lower value. This explains the shift of the emission contribution towards lower pressures. Unfortunately, the limited spectral range of the K-band makes these types of observations less sensitive to $\log g$. The surface gravity, metallicity, and effective temperature govern the atmospheric gaseous optical depth of an object. Since the atmospheric scale height is inversely proportional to the surface gravity, the latter influences the pressure range of the photosphere. Therefore, it plays a significant role in shaping the observed spectra as it affects line shapes, temperature profiles, and the overall continuum (Marley & Robinson, 2015; Mukherjee et al., 2024). González Picos et al. (2024) show that the posterior distributions of surface gravities

and metallicities exhibit a high degree of degeneracy in the K-band, as we also notice for our targets, hampering an accurate constraint.

2.5.5 Rotational velocity

J0835 has a rotational velocity of

$$v \sin i_{\mathrm{J0835}} = 15.42^{+0.14}_{-0.12} \text{ km s}^{-1}.$$

It is the fastest rotator of our small sample, as is also apparent from the broadened spectral features in Fig. 2.2. Blake et al. (2010) reported a similar value for the projected rotational velocity of $v \sin i_{\mathrm{J0835}} = 14.18 \pm 0.43$ km s^{-1}. For J0500 we retrieve a value of

$$v \sin i_{\mathrm{J0500}} = \ 5.05^{+0.21}_{-0.16} \text{ km s}^{-1},$$

while Blake et al. (2010) finds $v \sin i_{\mathrm{J0500}} = 9.65 \pm 0.36$ km s^{-1}. A possible explanation for this difference could be that their lower spectral resolution of $R \sim 35000$ hinders the measurement of low projected rotational velocities.

J0501 has a retrieved projected rotational velocity of

$$v \sin i_{\mathrm{J0501}} = 6.90^{+0.25}_{-0.24} \text{ km s}^{-1},$$

which is also lower than the velocity found by Vos et al. (2020), $9.57^{+0.67}_{-0.58}$ km s^{-1}, which was based on Gemini Near-InfraRed Spectrograph (GNIRS; Elias et al., 2006) high-resolution observations with $R \sim 18000$. Again, the higher resolution of our CRIRES+ observations likely aids in resolving such a low rotational velocity.

The projected rotational velocities are consistent with the expected slow rotation of young, bloated BDs. However, their intrinsic rotation velocities also depend on viewing angle. Similar to González Picos et al. (2024), there is a tentative relation between our GP parameters and the $v \sin i$. Slower rotators exhibit smaller GP length-scales, ℓ, and larger amplitudes, a, compared to fast rotators. This is as expected from the fact that for fast rotators, differences between model and observations will be smeared out over more spectral pixels, resulting in lower GP amplitudes and larger length-scales.

2.6 Conclusions and future work

We analysed high-resolution CRIRES+ spectra for three young BDs, providing insights into their atmospheric composition. Their C/O ratios are somewhat higher than that of the Sun, which could be the result of oxygen sequestration. Their metallicities are also higher by a factor of a few compared to the Sun. However, uncertainties may be underestimated due to the known correlation with surface gravity, to which these K-band observations are not very sensitive.

Performing precise measurements of isotope ratios is a challenge. However, we were able to constrain the isotopic composition of the BDs. The ^{12}C/^{13}C ratios for J0835, J0501, and J0500 are 93^{+10}_{-10} (9.1σ), 155^{+56}_{-53} (3.0σ), and 117^{+20}_{-17} (6.8σ), respectively. All values suggest a slightly depleted ^{13}CO concentration compared to that of the local ISM.

The remaining observational data of the SupJup Survey are being analysed, including tens of other BDs and SJs, to constrain their C/O, $^{12}C/^{13}C$, and $^{16}O/^{18}O$ ratios.

Acknowledgements

W.M. acknowledges funding from NWO grant from the second round of the Planetary and Exoplanetary Science Programme (PEPSci-II). S.d.R. and I.S. acknowledge funding from NWO grant OCENW.M.21.010. We thank the SURF Cooperative (www.surf.nl) for the support in using the National Supercomputer Snellius using grant no. EINF-4556 and EINF-9460. This research has made use of the following software: `Astropy` (Astropy Collaboration et al., 2022), `corner` (Foreman-Mackey, 2016), `Matplotlib` (Hunter, 2007), `MultiNest` (Feroz et al., 2019), `NumPy` (Harris et al., 2020), `petitRADTRANS` (Mollière et al., 2019), `picaso` (Mukherjee et al., 2023), `PyAstronomy` (Czesla et al., 2019), and `PyMultiNest` (Buchner et al., 2014).

2.A Posterior distributions of atmospheric retrievals

Supplementary graphs and tables are stored and can be found in the Zenodo repository: https://zenodo.org/records/14713641

2.A.1 Atmospheric retrieval of J0835

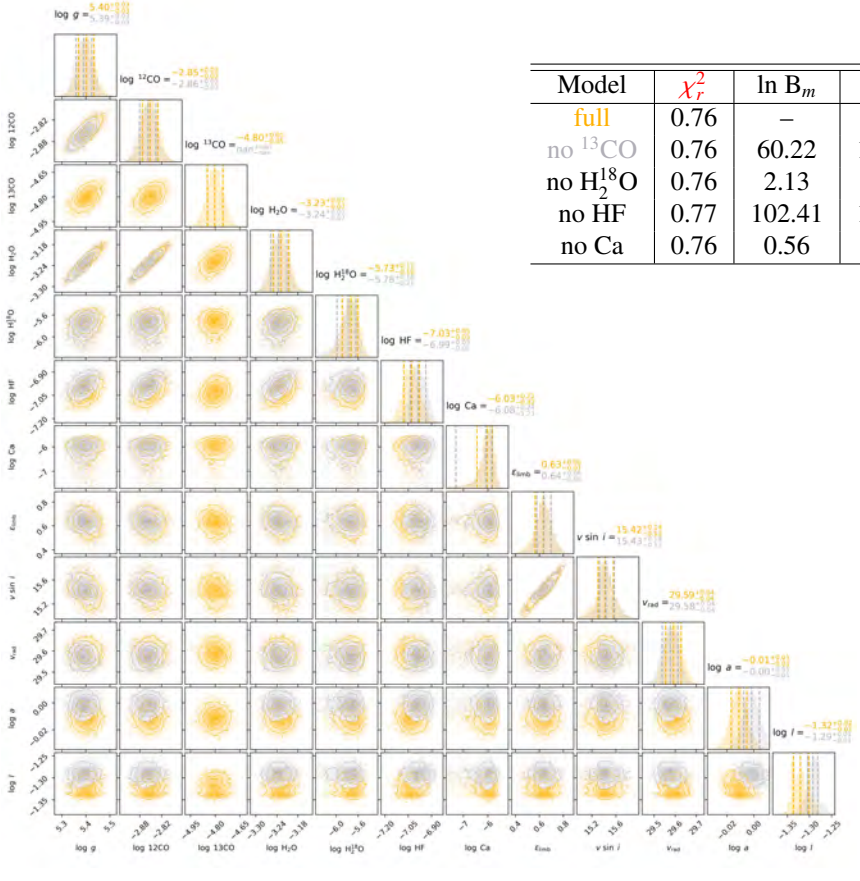

Model	χ^2_r	ln B_m	σ
full	0.76	–	–
no ^{13}CO	0.76	60.22	11.20
no $H_2^{18}O$	0.76	2.13	2.60
no HF	0.77	102.41	14.50
no Ca	0.76	0.56	1.72

Figure 2.8: Posterior distributions of the retrieved parameters for J0835. In yellow, we show the distributions for a model fitted for 21 free parameters including ^{12}CO, ^{13}CO, $H_2^{16}O$, $H_2^{18}O$, HF and Ca. The grey distributions represent a model where ^{13}CO is excluded. The reduced chi-squared values for the models with and without ^{13}CO, $H_2^{18}O$, HF and Ca are shown in the top right corner.

2.A.2 Atmospheric retrieval of J0501

Model	χ^2_r	ln B_m	σ
full	0.56	–	–
no ^{13}CO	0.58	6.62	4.06
no $H_2^{18}O$	0.56	-0.35	1.00
no HF	0.57	7.17	4.20
no Ca	0.57	0.31	1.50

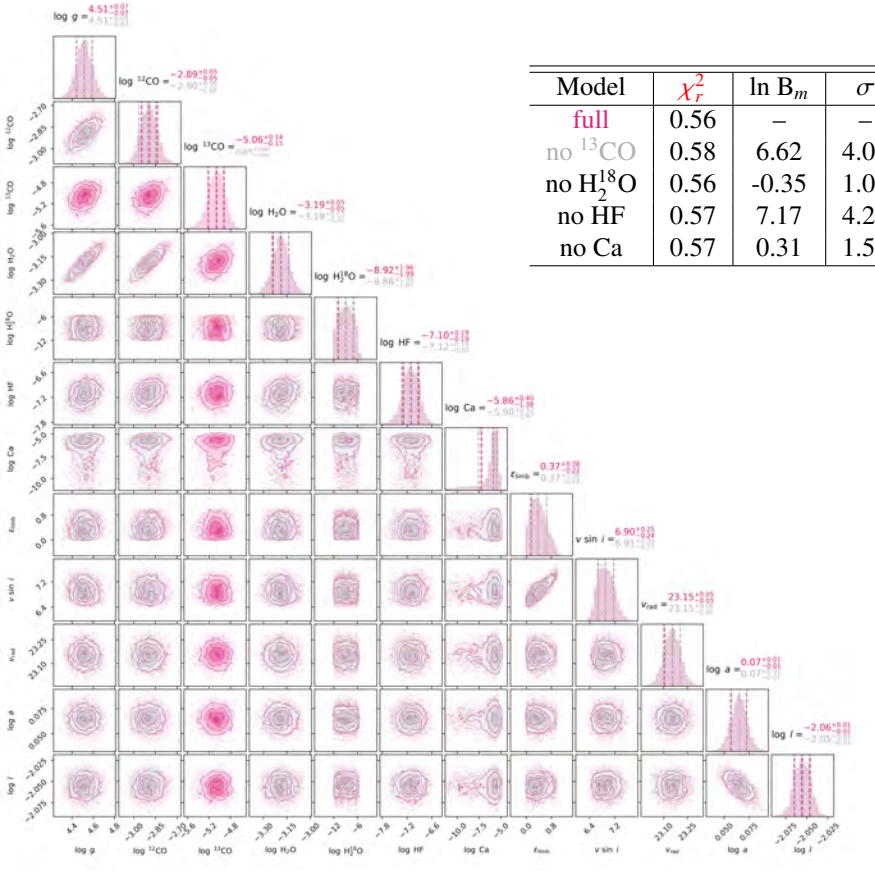

Figure 2.9: Posterior distributions of the retrieved parameters for J0501. In pink, we show the distributions for a model fitted for 21 free parameters including ^{12}CO, ^{13}CO, $H_2^{16}O$, $H_2^{18}O$, HF and Ca. The grey distributions represent a model where ^{13}CO is excluded. The reduced chi-squared values for the models with and without ^{13}CO, $H_2^{18}O$, HF and Ca are shown in the top right corner.

2.A.3 Atmospheric retrieval of J0500

Model	χ^2_r	ln B_m	σ
full	0.43	–	–
no ^{13}CO	0.43	19.99	6.64
no $H_2^{18}O$	0.43	0.00	0.00
no HF	0.43	39.64	9.16
no Ca	0.43	1.07	2.07

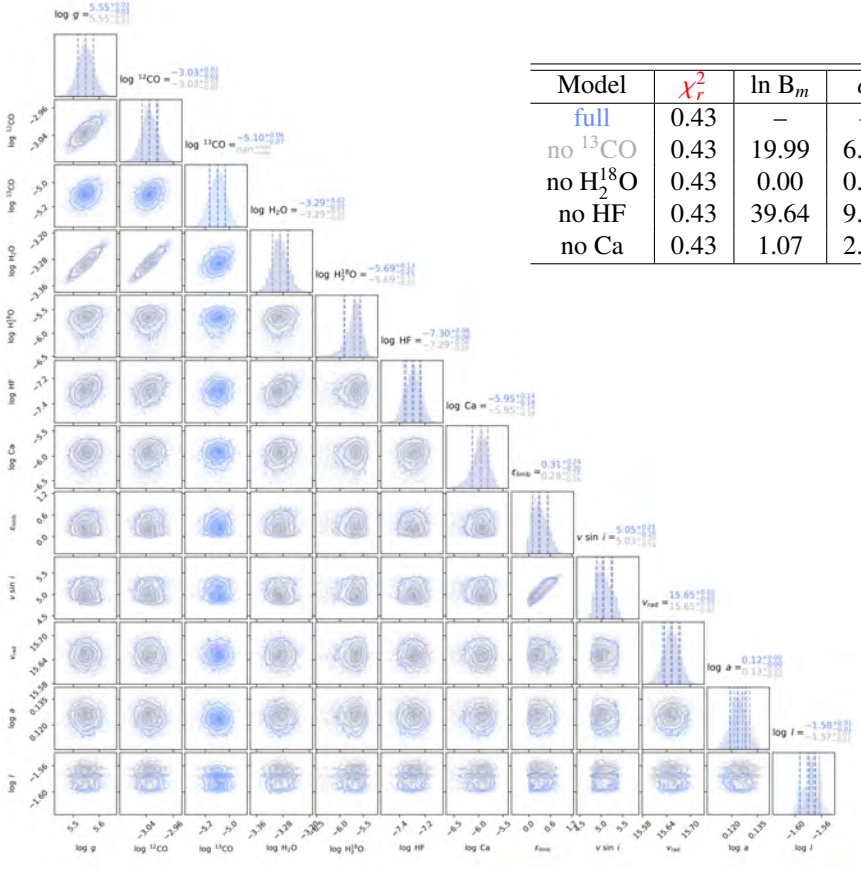

Figure 2.10: Posterior distributions of the retrieved parameters for J0500. In blue, we show the distributions for a model fitted for 21 free parameters including ^{12}CO, ^{13}CO, $H_2^{16}O$, $H_2^{18}O$, HF and Ca. The grey distributions represent a model where ^{13}CO is excluded. The reduced chi-squared values for the models with and without ^{13}CO, $H_2^{18}O$, HF and Ca are shown in the top right corner.

2.B Best Fitting Spectra

Supplementary graphs and tables are stored and can be found in the Zenodo repository: https://zenodo.org/records/14713641

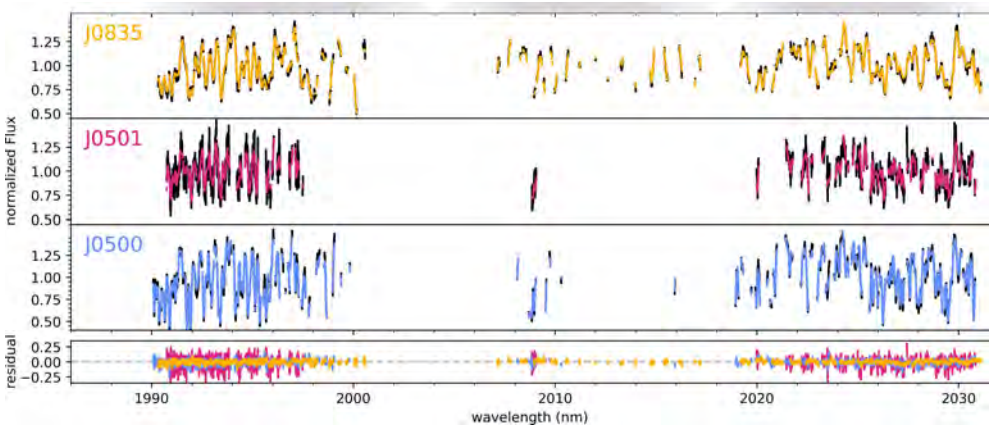

Figure 2.11: Best-fitting models of 2nd K2166 order (upper three panels) retrieved for J0835, J0501 and J0500 (top to bottom) plotted on top of the observational flux in black. This order contains many masked telluric lines, resulting in large gaps in the data.

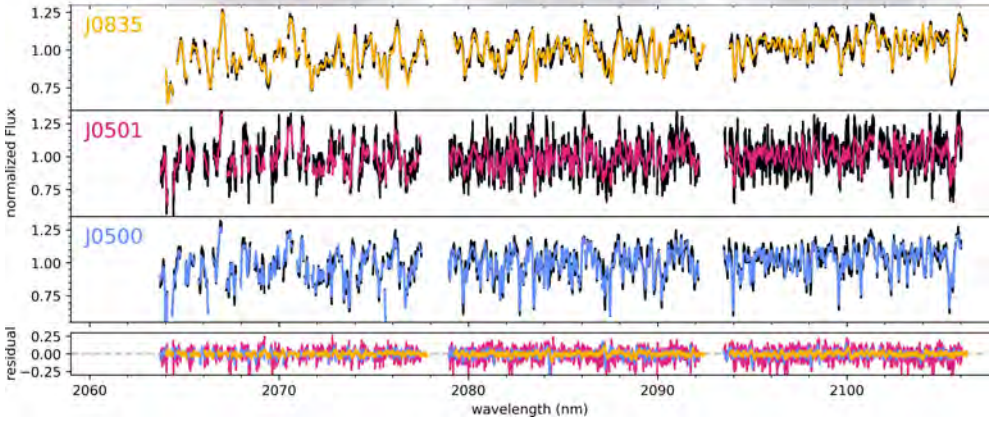

Figure 2.12: Best-fitting models of 3rd K2166 order (upper three panels) retrieved for J0835, J0501 and J0500 (top to bottom) plotted on top of the observational flux in black.

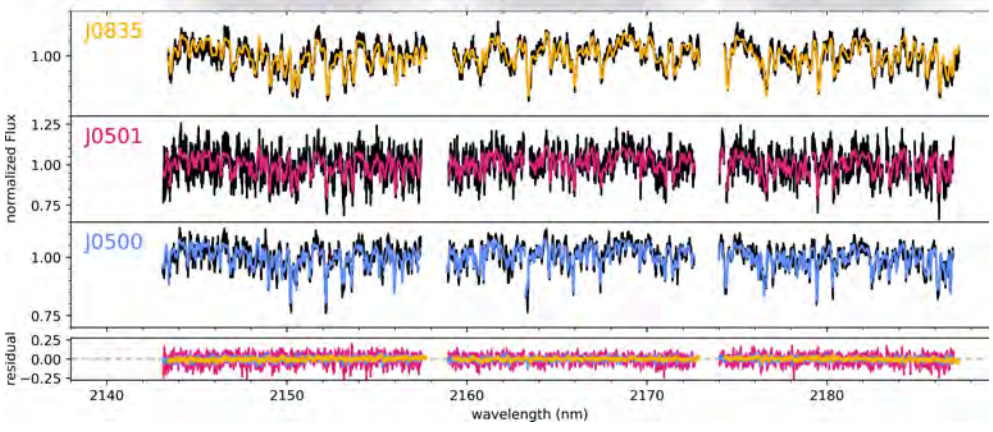

Figure 2.13: Best-fitting models of 4th K2166 order (upper three panels) retrieved for J0835, J0501 and J0500 (top to bottom) plotted on top of the observational flux in black.

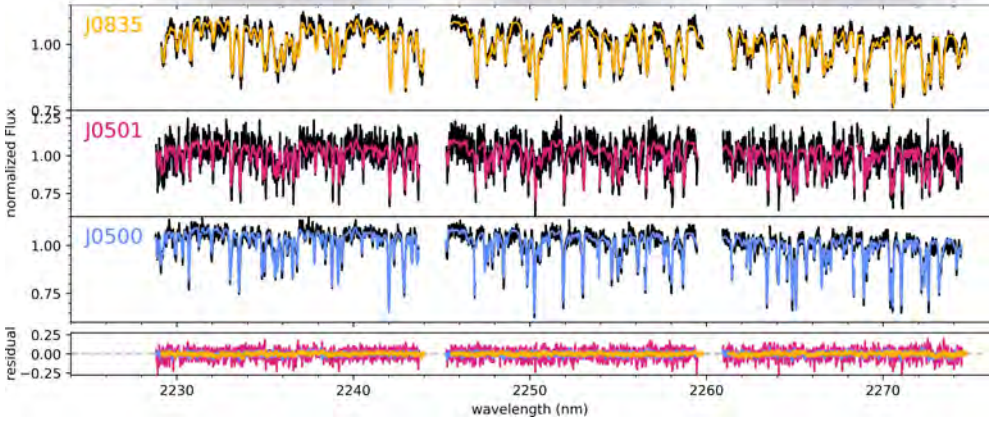

Figure 2.14: Best-fitting models of 5th K2166 order (upper three panels) retrieved for J0835, J0501 and J0500 (top to bottom) plotted on top of the observational flux in black.

2.C Cross-correlation analysis of ^{12}CO, ^{13}CO, $H_2^{16}O$, $H_2^{18}O$, HF, and Ca abundances

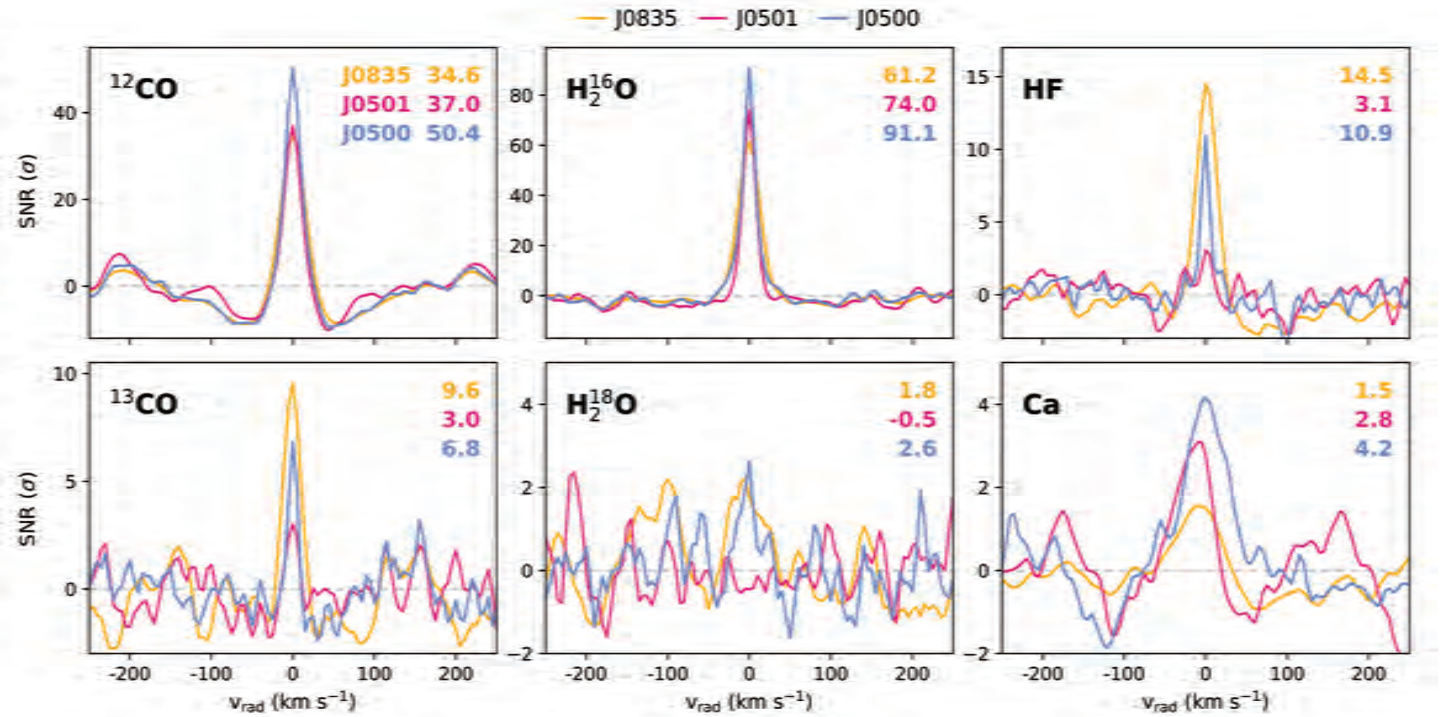

Figure 2.15: CCFs for ^{12}CO, ^{13}CO, $H_2^{16}O$, $H_2^{18}O$, HF, and Ca abundances. The CCFs were calculated for each order–detector pair and summed over all orders and detectors, after which they were converted to S/Ns by dividing by the standard deviation of the CCFs in the range $|v_{\rm rad}| > 100$ km s^{-1}. The different colours represent the different targets, J0835, J0501, and J0500. The peaks at $v_{\rm rad} = 0$ km s^{-1} are a result of the cross-correlation being performed on the observed spectrum centred in its rest frame. We indicate the peak S/N values in units of σ for each species and BD in the upper-right corner.